nanomaterials

MDPI

Article

CO_2 Utilization and Sequestration in Organic and Inorganic Nanopores During Depressurization and Huff-n-Puff Process

Jiadong Guo [1], Shaoqi Kong [1,*], Kunjie Li [2], Guoan Ren [3], Tao Yang [4], Kui Dong [1] and Yueliang Liu [5,6,7,*]

[1] College of Mining Engineering, Taiyuan University of Technology, Taiyuan 030024, China; 18536201839@163.com (J.G.); dongkui@tyut.edu.cn (K.D.)
[2] State Key Laboratory of Coaland CBM Co-Mining, Taiyuan 030032, China; marden2008@163.com
[3] Jin Chuang Investment Co., Ltd., Taiyuan 030000, China; rga78919@163.com
[4] School of Mine Safety, North China Institute of Science and Technology, Beijing 101601, China; yangtao585@163.com
[5] State Key Laboratory of Petroleum Resources and Prospecting, China University of Petroleum (Beijing), Beijing 102249, China
[6] College of Petroleum Engineering, China University of Petroleum (Beijing), Beijing 102249, China
[7] College of Carbon Neutrality Future Technology, China University of Petroleum (Beijing), Beijing 102249, China
* Correspondence: kongshaoqi@tyut.edu.cn (S.K.); yueliang@cup.edu.cn (Y.L.)

Abstract: CO_2 injection in shale reservoirs is more suitable than the conventional recovering methods due to its easier injectivity and higher sweep efficiency. In this work, Grand Canonical Monte Carlo (GCMC) simulation is employed to investigate the adsorption/desorption behavior of CH_4-C_4H_{10} and CH_4-C_4H_{10}-CO_2 mixtures in organic and inorganic nanopores during pressure drawdown and CO_2 huff and puff processes. The huff and puff process involves injecting CO_2 into the micro- and mesopores, where the system pressure is increased during the huffing process and decreased during the puffing process. The fundamental mechanism of shale gas recovery using the CO_2 injection method is thereby revealed from the nanopore-scale perspective. During primary gas production, CH_4 is more likely to be produced as the reservoir pressure drops. On the contrary, C_4H_{10} tends to be trapped in these organic nanopores and is hard to extract, especially from micropores and inorganic pores. During the CO_2 huffing period, the adsorbed CH_4 and C_4H_{10} are recovered efficiently from the inorganic mesopores. On the contrary, the adsorbed C_4H_{10} is slightly extracted from the inorganic micropores during the CO_2 puffing period. During the CO_2 puff process, the adsorbed CH_4 desorbs from the pore surface and is thus heavily recovered, while the adsorbed C_4H_{10} cannot be readily produced. During CO_2 huff and puff, the recovery efficiency of CH_4 is higher in the organic pores than that in the inorganic pores. More importantly, the recovery efficiency of C_4H_{10} reaches the highest levels in both the inorganic and organic pores during the CO_2 huff and puff process, suggesting that the CO_2 huff and puff method is more advanced for heavier hydrocarbon recovery compared to the pressure drawdown method. In addition to CO_2 storage, CO_2 sequestration in the adsorbed state is safer than that in the free state. In our work, it was found that the high content of organic matter, high pressure, and small pores are beneficial factors for CO_2 sequestration transforming into adsorbed state storage.

Keywords: shale gas; pressure drawdown; organic nanopores; CO_2 huff and puff; CO_2 sequestration

check for updates

Citation: Guo, J.; Kong, S.; Li, K.; Ren, G.; Yang, T.; Dong, K.; Liu, Y. CO_2 Utilization and Sequestration in Organic and Inorganic Nanopores During Depressurization and Huff-n-Puff Process. *Nanomaterials* **2024**, *14*, 1698. https://doi.org/10.3390/nano14211698

Academic Editor: Diego Cazorla-Amorós

Received: 19 September 2024
Revised: 10 October 2024
Accepted: 15 October 2024
Published: 24 October 2024

Copyright: © 2024 by the authors. Licensee MDPI, Basel, Switzerland. This article is an open access article distributed under the terms and conditions of the Creative Commons Attribution (CC BY) license (https://creativecommons.org/licenses/by/4.0/).

1. Introduction

The potential for shale oil resources in China's saline lake sediments is huge [1], which makes shale oil an important energy type, as the output of traditional fuels is declining sharply [2–5]. Although the original reserves of shale oil are abundant all over the world, commercially recoverable shale is quite limited due to its distinctive characteristics, such as extremely low permeability, etc. [6,7]. In recent years, horizontal drilling and multi-staged

hydraulic fracturing have been widely recognized as the main technologies for shale oil production [8]. Although shale oil can be recovered at the initial stage after employing these developing methods, large amounts of shale resources are still left in shale reservoirs, up to 80% [9,10]. More advanced technologies should be developed to enhance shale oil recovery. There is a strong motivation for developing advanced extraction technologies in that even a 1.0% increase in oil recovery results in the production of an extra 1.6–9.0 billion barrels of oil [11].

Gas injection is accepted as being more advanced than traditional technologies for shale recovery. Gas is superior at entering the nanopores and therein has a higher sweep efficiency in shale reservoirs. Commonly used gases in oilfields are N_2, CO_2, natural gas, etc., of which CO_2 possesses the lowest minimum miscibility pressure (MMP) compared to other gases [12,13]. The basic mechanism of CO_2 for oil recovery includes oil swelling and considerable oil viscosity reduction [14–18]. When injected, CO_2 can become miscible with the crude oil when the pressure is higher than the MMP. However, the miscible conditions are not easy to achieve in shale reservoirs. In fact, the light and intermediate hydrocarbons are readily recovered by CO_2, while the heavy components remain in nanopores and are hard to recover [19].

Recently, methane, propane, butane, etc., have been proposed as cosolvents to assist CO_2 for oil recovery, through which the performance of CO_2 is reinforced [20–23]. With the assistance of a cosolvent, the miscibility performance of CO_2 is greatly improved in the in situ oil; in addition, a cosolvent can also dissolve and reduce the viscosity of crude oil, which is beneficial for oil recovery. Methanol is used with CO_2 to remove the liquid blockage in unconventional condensate reservoirs [24,25]. Liu et al. (2022) proposed dimethyl ether to assist CO_2 flooding for oil recovery, as well as carbon sequestration, so-called storage-driven CO_2 enhanced oil recovery (EOR) [26,27]. In order to improve shale oil recovery, more advanced technologies need to be developed. Hydrochloric saline lake shale formations are dominated by inorganic pores and have a low incidence of organic pores [28], which is of great significance for the design of CO_2 injection wells. In order to improve the design of CO_2 injection, it is critical to have a basic understanding of the fundamental mechanisms of shale hydrocarbon recovery during CO_2 injection [29–39]. Advanced heating technologies like radio frequency and microwave heating can enhance carbon dioxide removal and recovery, improving energy efficiency and environmental sustainability. J.F. et al. demonstrated that radiofrequency(RF)-heated fixed-bed reactors utilizing $CaCO_3$ sorbent can enhance CO_2 capture from flue gas [40], while T.C. et al. found that Microwave Swing Desorption (MSD) accelerates CO_2 desorption from microporous activated carbon fourfold compared to Temperature Swing Desorption (TSD) [41], together, showcasing innovative approaches to improving CO_2 management and emissions reduction.

In this work, the Grand Canonical Monte Carlo (GCMC) simulation method is employed to investigate the adsorption/desorption behavior of CH_4-C_4H_{10} and CH_4-C_4H_{10}-CO_2 mixtures in organic and inorganic nanopores during pressure drawdown and CO_2 huff and puff processes. Specifically, the influence of pore size, mineral types of nanopores, and pressure on adsorption and desorption behavior are thoroughly evaluated. The fundamental mechanism of shale gas recovery using the CO_2 injection method is thereby revealed from the nanopore-scale perspective. This study enhances the understanding of CO_2 injection in shale oil and gas recovery, offering a theoretical foundation for optimizing extraction technologies. By examining adsorption and desorption behaviors in nanopores, the research improves recovery efficiency and promotes sustainability. Additionally, the findings contribute to emission reduction, carbon sequestration, and the global energy crisis, supporting energy transition. Overall, the research holds significant academic value and potential applications, benefiting national energy security and environmental protection.

2. Molecular Models and Simulations

The mineral analysis indicates that Chang 7 shale is rich in organic kerogen and K-illite. The surface morphology of Chang 7 shale suggests that the shape morphology of

the nanopores can be simplified as slit-shaped in the molecular models. The organic pore is usually represented by the carbon-based pore. In this molecular model, the carbon-slit pore is employed to represent the kerogen nanopore for simplicity, i.e., organic pores; the K-illite nanopore is used to represent the inorganic nanopore. In this study, the inorganic characteristics of the pores are predominantly influenced by the structural features of K-illite, known for its stable crystal framework and high thermal resistance. Conversely, the organic pores are derived from the organic kerogen-rich Chang 7 shale, which demonstrates excellent adsorption capacity and chemical reactivity. Consequently, both the inorganic and organic pores possess distinct advantages in terms of functionality and properties, collectively impacting the physicochemical performance of the shale. It should be noted that the K-illite has one Al-O octahedral sheet lying between each of the two Si-O tetrahedral sheets, i.e., one typical 2:1 clay mineral for Chang 7 shale [42]. The K-illite has the unit cell formula $K_x[Al_xSi_{(8-x)}][Al_yMg_{4-y}]O_{20}(OH)_4$ [43], in which the x and y represent 1 and 4, respectively. The clay sheet is negatively charged because one Si^{4+} cation is usually replaced by one Al^{3+} cation in every unit cell. Meanwhile, in the interlayers, the K^+ cations are distributed randomly, counterbalancing the negative charges in the unit cell. It is noted that we investigate the recovery mechanism of shale gas in organic and inorganic nanopores with two sizes, i.e., 1 nm and 3 nm, representing micropores and mesopores, respectively.

The force field is used for the potential models of adsorbed gas [44]. The clay models are obtained from the CLAYFF force field. The C and H atoms in the alkanes are regarded as a united atom, while the partial charge of the C atom and O atoms in the CO_2 molecule are taken as +0.7e and −0.35e, respectively. The following potential model is used to describe the Lennard-Jones (LJ) potential and the electrostatic terms for the nonbonded interactions:

$$u(r_{ij}) = 4\varepsilon_{ij}\left[\left(\frac{\sigma_{ij}}{r_{ij}}\right)^{12} - \left(\frac{\sigma_{ij}}{r_{ij}}\right)^{6}\right] + \frac{q_i q_j}{4\pi\varepsilon_0 r_{ij}} \quad (1)$$

where ε_{ij} is the well depth of the LJ potential, and the σ_{ij} is the LJ radius; r_{ij} is the distance between atoms i and j; and q represents the atrial atom charge, which is employed to calculate the Coulomb interactions.

The cross interactions between two different atoms are calculated by the Lorentz–Berthelot combining rules as follows [45]:

$$\sigma_{ij} = \frac{1}{2}(\sigma_{ii} + \sigma_{jj}) \quad (2)$$

$$\varepsilon_{ij} = \sqrt{\varepsilon_{ii}\varepsilon_{jj}} \quad (3)$$

The Ewald summation method is used to estimate the long-range electrostatic interactions by placing a vacuum slab in the z direction in the simulation cell [46,47].

In this study, the adsorption and desorption behavior of alkane/CO_2 mixtures is investigated by the GCMC simulation method. The grand canonical μVT ensemble is employed in this work, where μ, V, and T represent the chemical potentials, volume, and temperature, respectively; within such an ensemble, μ, V, and T are regarded as constants [48]. Within the molecular simulation, gas molecules in nanopores can exchange with a fictitious bulk reservoir with a fixed chemical potential. At the beginning of constructing the GCMC simulation, we set the starting point of the simulation by selecting a certain number of C_4H_{10} and CO_2 molecules and randomly distributing them in the nanopores to represent the initial state. This initial configuration undergoes multiple cycles of energy minimization to ensure the thermodynamic stability of the system. A configurational-biased GCMC algorithm is used to insert and remove C_4H_{10} molecules from nanopores [48]. The chemical potentials of bulk CH_4 and C_4H_{10} molecules in the canonical ensemble are calculated using Widom's insertion method [49]. During GCMC simulations, the nanopore structure is fixed. The transitional move is implemented with CH_4 molecules, which removes them from or inserts them into the simulation box randomly, with equal probability. As for CO_2 and

C_4H_{10}, in addition to the transitional move, a rotational move is implemented [48]. The Peng–Robinson equation of state (PR-EOS) is used to calculate the bulk densities [50]. The gas molecules are endowed with an equal probability; according to the chemical potential of the bulk reservoir, the gas molecules can be inserted or removed from the nanopores. The bulk reservoir has a given pressure and temperature. In order to initiate gas production, the bulk pressure is lowered from the initial pressure (P_i = 400 bar) to P_1 = 200 bar and P_3 = 100 bar. The equilibrium pressure (P_2) in the nanopores after gas injection is calculated using the PR-EOS [50]. The equilibrium fluid composition is calculated based on the chemical potentials in and out of the nanopores.

As for the depressurization and CO_2 huff-n-puff processes performed by GCMC, the primary pressure drawdown is first performed to initiate shale hydrocarbon production by lowering the bulk pressure from P_i = 400 bar to P_1 = 200 bar. Subsequently, CO_2 is introduced into the bulk volume. The PR-EOS is used to calculate the equilibrium pressure after CO_2 injection, i.e., P_2 [50]. After reaching equilibrium, the puffing process, i.e., a pressure drawdown process, is applied, starting from P_2 to P_3 = 100 bar. In order to achieve equilibrium, 0.3 million cycles are required for each molecule and 0.7 million cycles are required for sampling. This timescale ensures the stability and accuracy of the simulation process.

Through statistical analysis and comparison of the simulation results, we validated the effectiveness of the GCMC simulation method, which provides a solid theoretical foundation and an experimental basis for a deeper understanding of the adsorption and desorption behaviors of alkane/CO_2 mixtures.

3. Results and Discussion

3.1. Primary Production during Depressurization

3.1.1. Organic Nanopores

Figures 1–4 present the density distribution of CH_4, C_4H_{10}, and CH_4-C_4H_{10} mixtures in the micropores and mesopores at P_i and P_1, respectively. It is noted that carbon slit pores were employed to represent the organic pores in shale, considering that carbon slit has similar physical properties to that of the organic matter in shale. In the micropores and mesopores, the density of hydrocarbons near the surface was significantly higher than that in the pore center, indicating that hydrocarbons form adsorption layers on the pore surface, while hydrocarbon molecules tended to stay in a free-gas state due to the relatively weak surface attraction. In addition, the density of hydrocarbons in the adsorption layers was remarkably higher than that in the mesopores due to the coupling effect of surface attraction from both sides of the nanopores. The density at the pore center of mesopores approached the bulk density, indicating that the gas readily formed free gas in the mesopores. However, the density at the pore center of the micropores did not converge with the bulk density, suggesting that there was no free-gas region.

As shown in Figures 1 and 2, the density of CH_4 decreases both in the adsorption layers and at the center of nanopores as the pressure declines. However, there is no obvious density change for C_4H_{10} whether in the micropores or in the mesopores. In addition, for CH_4-C_4H_{10} mixtures, the density of CH_4 drops in the first adsorption layer as pressure decreases, while C_4H_{10} shows enrichment near the pore surface during pressure drawdown, indicated by increasing density at a lower pressure. During the primary gas production, the lighter hydrocarbons are more likely desorbed from the pore surface and more easily produced as the reservoir pressure drops, like CH_4. On the contrary, due to the stronger interaction with the pore surface, the heavier components tend to be trapped in these organic nanopores, especially in micropores. This behavior is similar to that found in other adsorbents, such as zeolites [51] and graphene [52,53].

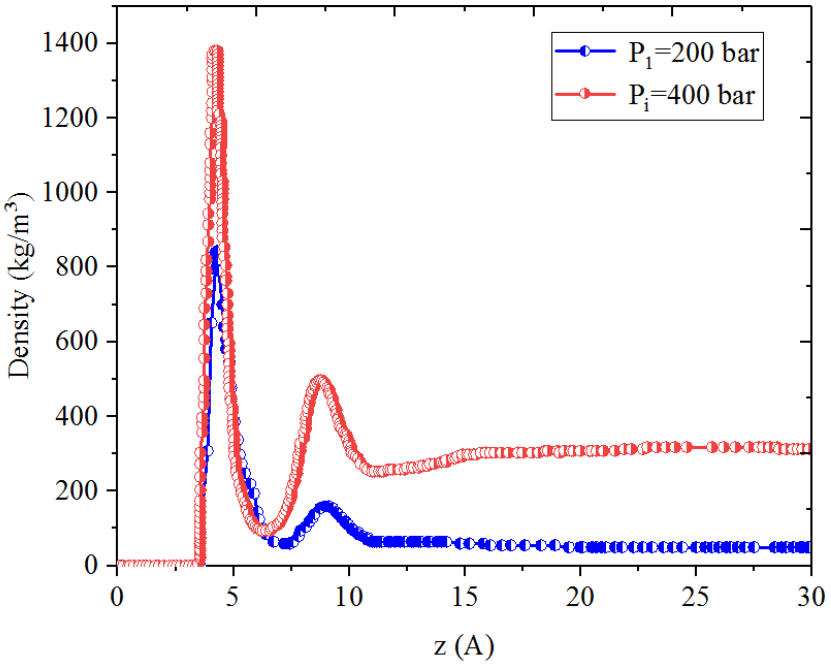

Figure 1. Density profiles of CH_4 in CH_4-C_4H_{10} mixture in organic mesopores at 353.15 K.

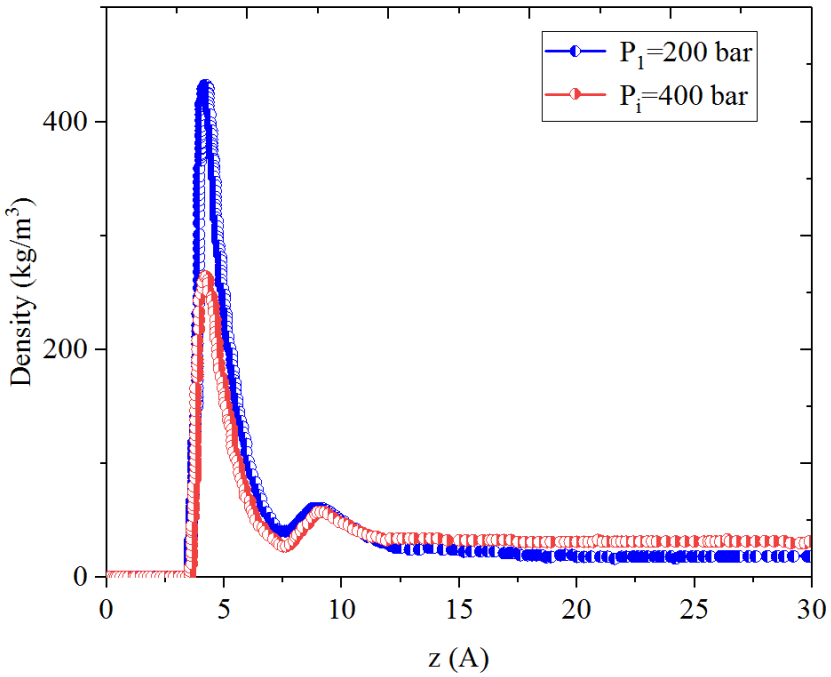

Figure 2. Density profiles of C_4H_{10} in CH_4-C_4H_{10} mixture in organic mesopores at 353.15 K.

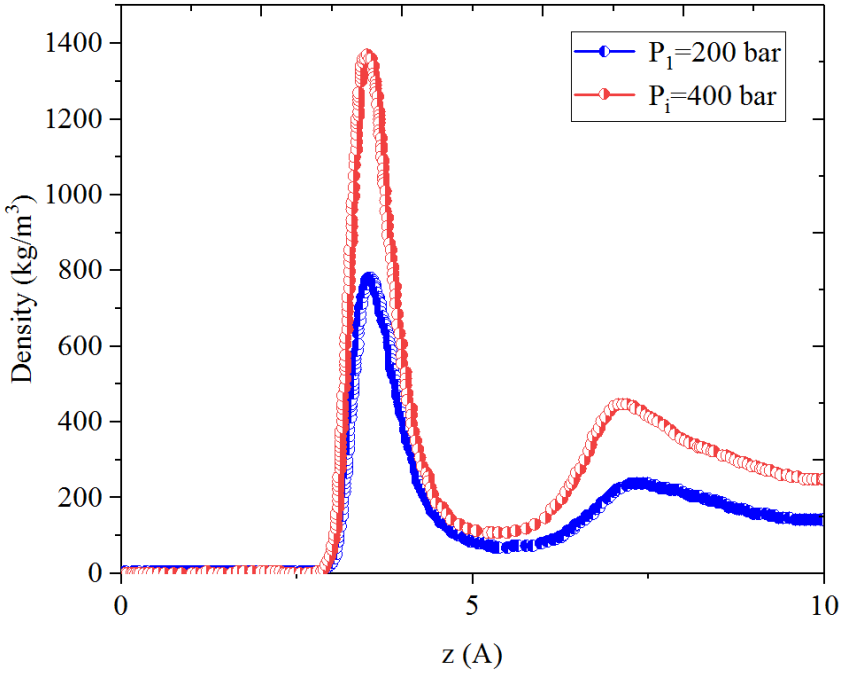

Figure 3. Density profiles of CH_4 in CH_4-C_4H_{10} mixture in organic micropores at 353.15 K.

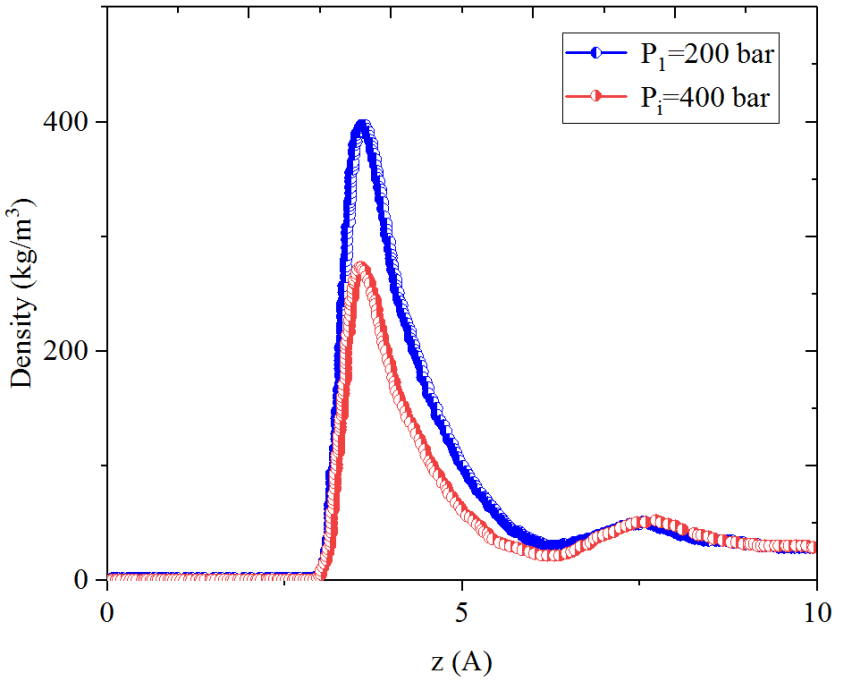

Figure 4. Density profiles of C_4H_{10} in CH_4-C_4H_{10} mixture in organic micropores at 353.15 K.

3.1.2. Inorganic Nanopores

Figures 5–8 present the density distribution of CH_4 and C_4H_{10} in a CH_4-C_4H_{10} mixture in the inorganic micropores and mesopores at P_i and P_1, respectively. In this work, the inorganic nanopores are represented by K-illite pores. Similarly to that in the organic pores, CH_4 and C_4H_{10} molecules form an adsorption layer near the pore surface and free-gas region at the pore center in mesopores, while there is no free gas in the micropores. Comparatively, the density in the adsorption layers in the inorganic pores is much smaller than that in the organic pores, demonstrating relatively weaker molecule–surface interactions in the inorganic pores. As the pressure drops, the density of CH_4 in the adsorption layer

decreases, while the adsorption layer of C_4H_{10} cannot be recovered during pressure drawdown. Specifically, as with the CH_4-C_4H_{10} mixture, the density of C_4H_{10} increases in the first adsorption layer, and the increase is remarkably more significant in the inorganic pores than that of the organic nanopores. In other words, it is more difficult to recover the heavier hydrocarbons from the inorganic pores, such as C_4H_{10}.

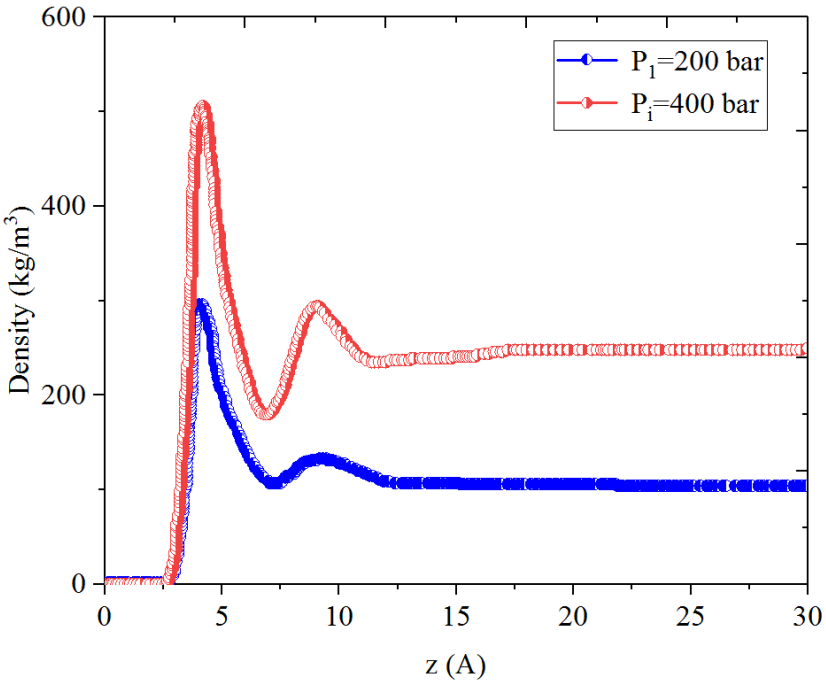

Figure 5. Density profiles of CH_4 in CH_4-C_4H_{10} mixture in inorganic mesopores at 353.15 K.

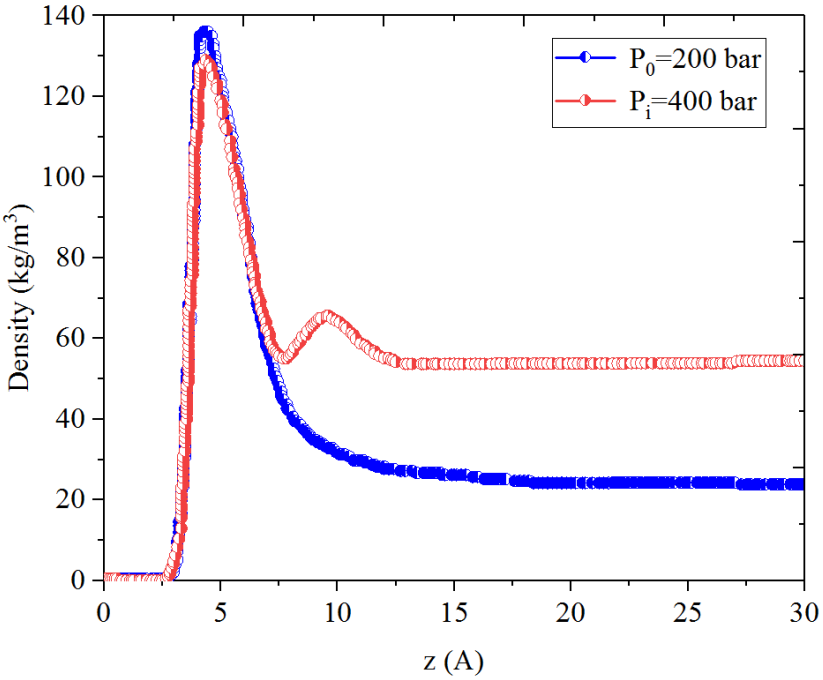

Figure 6. Density profiles of C_4H_{10} in CH_4-C_4H_{10} mixture in inorganic mesopores at 353.15 K.

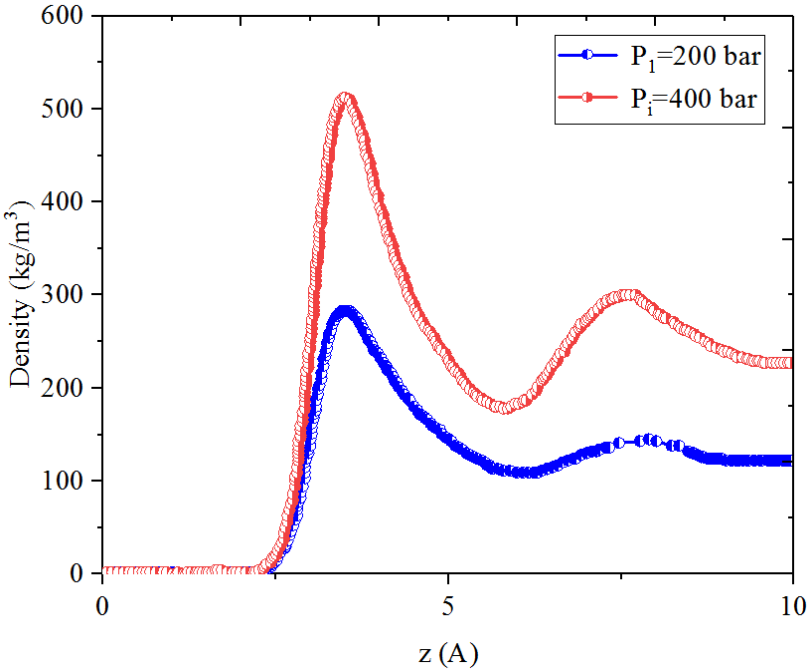

Figure 7. Density profiles of CH_4 in CH_4-C_4H_{10} mixture in inorganic micropores at 353.15 K.

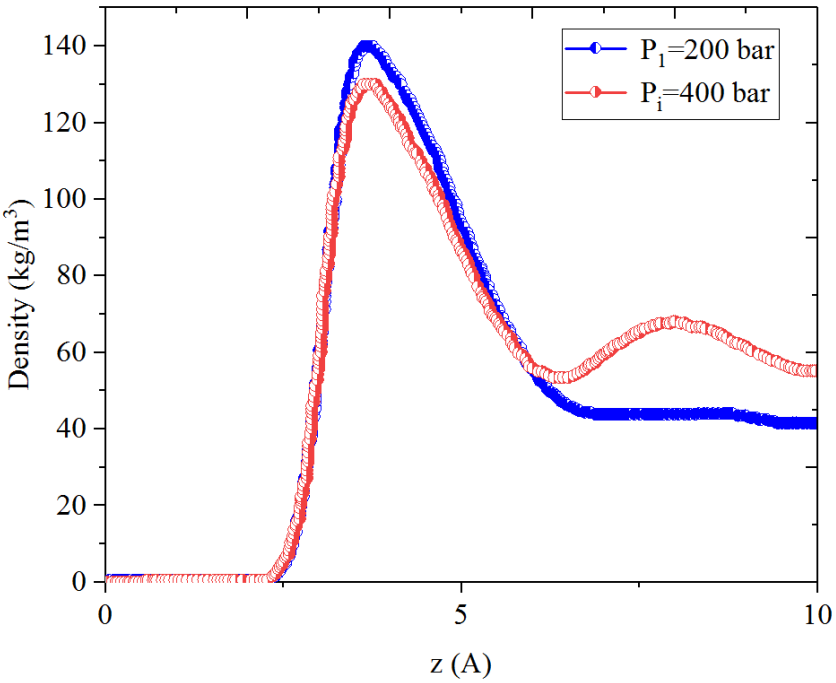

Figure 8. Density profiles of C_4H_{10} in CH_4-C_4H_{10} mixture in inorganic micropores at 353.15 K.

3.2. Improved Gas Production during CO_2 Huff-n-Puff Process

3.2.1. Organic Nanopores

In this process, CO_2 is injected into the micro- and mesopores; the system pressure is increased from P_1 to P_2 during the huffing process and then it decreases to P_3 in the puffing process. Figures 9–12 present the density profiles of CH_4 and C_4H_{10} in the CH_4-C_4H_{10} mixture in the organic micropores and mesopores at P_1, P_2, and P_3, respectively. Comparatively, CO_2 presents the strongest adsorption capacity on the pore surface compared to CH_4 and C_4H_{10}. In addition, it is found that the adsorption layer of CO_2 is much closer to the pore surface than those of the alkanes, i.e., CH_4 and C_4H_{10}. After introducing CO_2, i.e.,

in the CO_2 huffing period ($P_1 \rightarrow P_2$), the density in the first adsorption layer of CH_4 and C_4H_{10} decreases drastically, indicating that the adsorbed hydrocarbons are replaced by the injected CO_2. This observation agrees well with the previous work [19,54]. In the puffing process, i.e., $P_2 \rightarrow P_3$, the adsorbed CH_4 desorbs from the pore surface continuously and thus can be heavily recovered. However, the density of C_4H_{10} in the adsorption layer is slightly changed, suggesting that the adsorbed C_4H_{10} cannot be readily produced. More interestingly, as puffing time continues, the adsorbed CH_4 in the CH_4-C_4H_{10} mixture is produced as expected, while the density of C_4H_{10} in the adsorption layer increases, indicating that C_4H_{10} re-adsorbs on the pore surface in the huffing period.

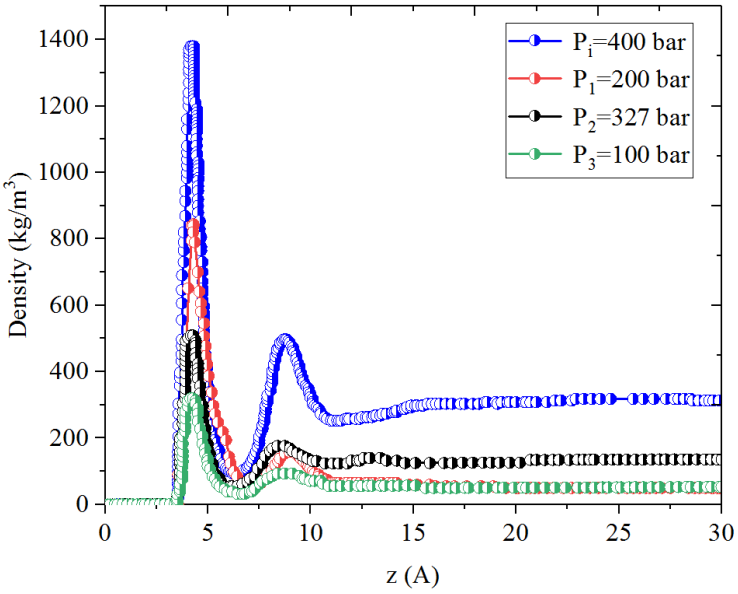

Figure 9. Density profiles of CH_4 in CH_4-C_4H_{10}-CO_2 mixture in organic mesopores at P_i, P_1, P_2, and P_3, respectively.

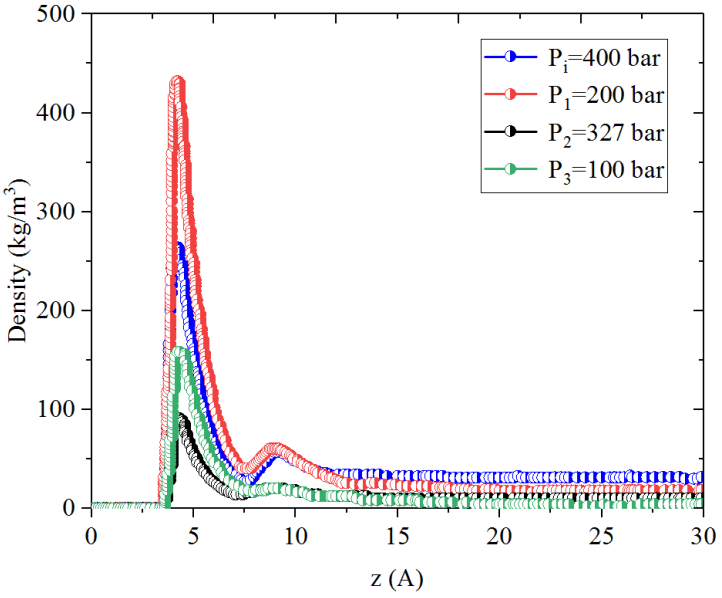

Figure 10. Density profiles of C_4H_{10} in CH_4-C_4H_{10}-CO_2 mixture in organic mesopores at P_i, P_1, P_2, and P_3, respectively.

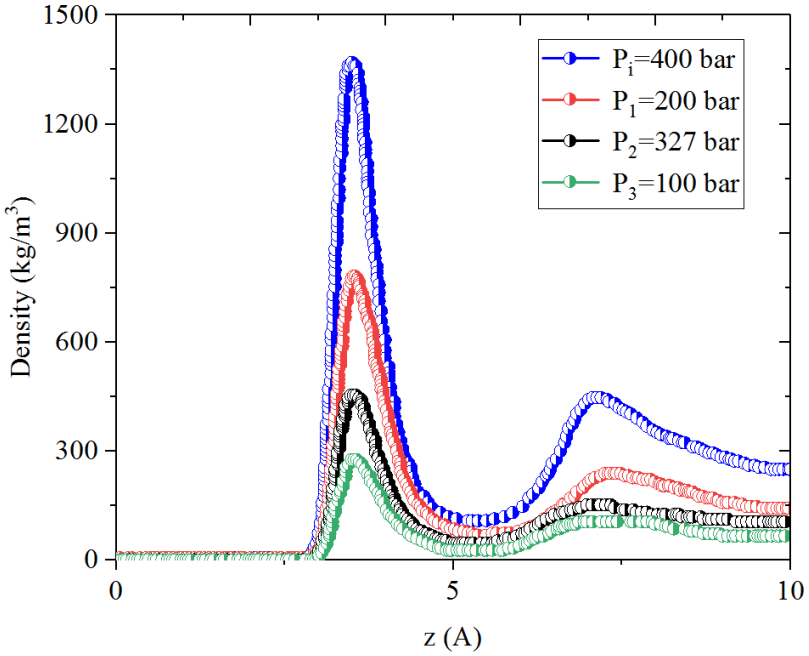

Figure 11. Density profiles of CH_4 in CH_4-C_4H_{10}-CO_2 mixture in organic micropores at P_i, P_1, P_2, and P_3, respectively.

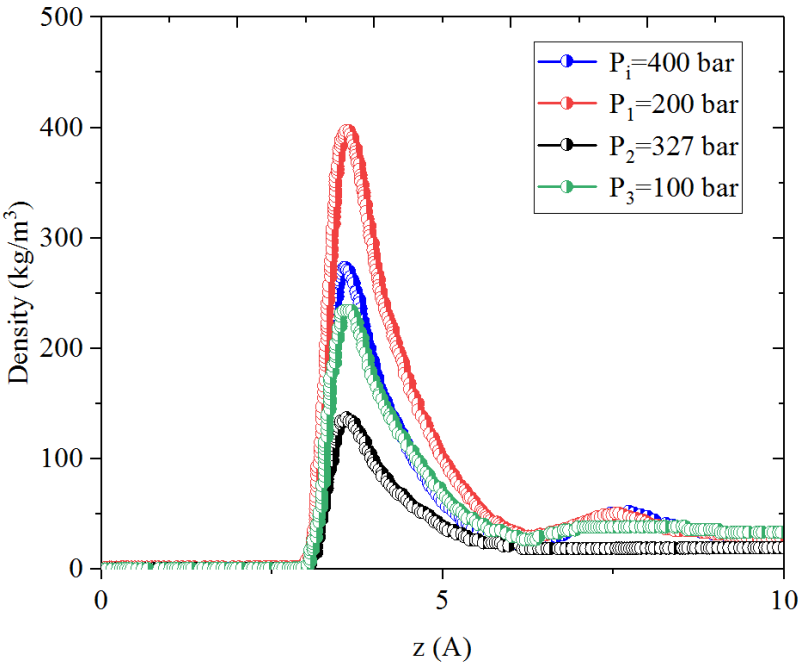

Figure 12. Density profiles of C_4H_{10} in CH_4-C_4H_{10}-CO_2 mixture in organic micropores at P_i, P_1, P_2, and P_3, respectively.

3.2.2. Inorganic Nanopores

Figures 13–16 present the density profiles of CH_4, C_4H_{10}, and the CH_4-C_4H_{10} mixture in the inorganic micropores and mesopores at P_1, P_2, and P_3, respectively. Unlike in organic pores, the density of CO_2 in the adsorption layer within inorganic pores is significantly higher. It was reported that CO_2 molecules have a neutral charge and zero dipole moment, while CO_2 molecules exhibit a strong quadrupole moment [55,56]. These properties enable CO_2 to have improved adsorption by combining with the charged clay atoms [46]. Due to the presence of CO_2 adsorption layers, CH_4 and C_4H_{10} form a second minor adsorption

layer towards the pore center. In the inorganic mesopores, the density of CH_4 and C_4H_{10} decreases significantly in the adsorption layer during the CO_2 huffing period. That is, the adsorbed CH_4 and C_4H_{10} can be recovered efficiently from the inorganic mesopores during the CO_2 huffing period. On the contrary, in the inorganic micropores, the density of C_4H_{10} in the adsorption layer slightly increases during the CO_2 puffing period.

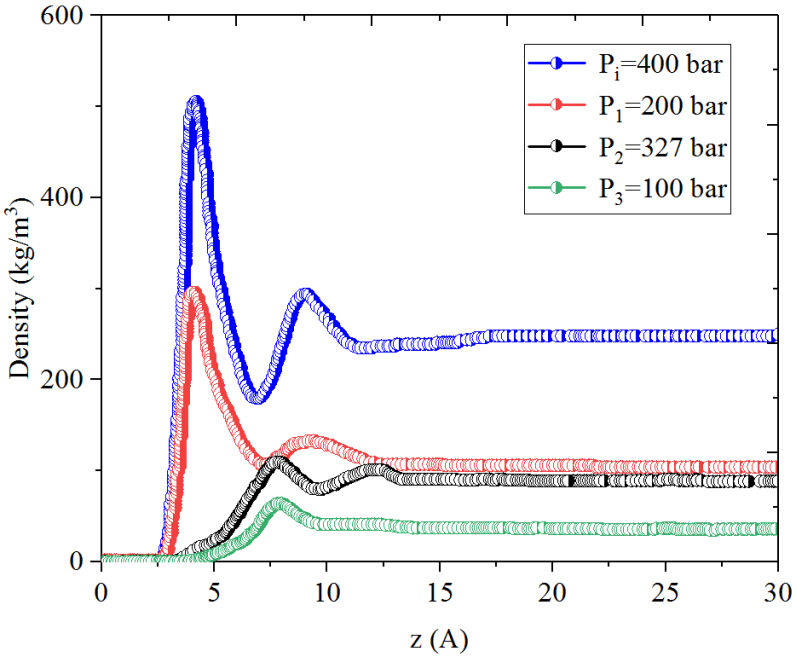

Figure 13. Density profiles of CH_4 in CH_4-C_4H_{10}-CO_2 mixture in inorganic mesopores at P_i, P_1, P_2, and P_3, respectively.

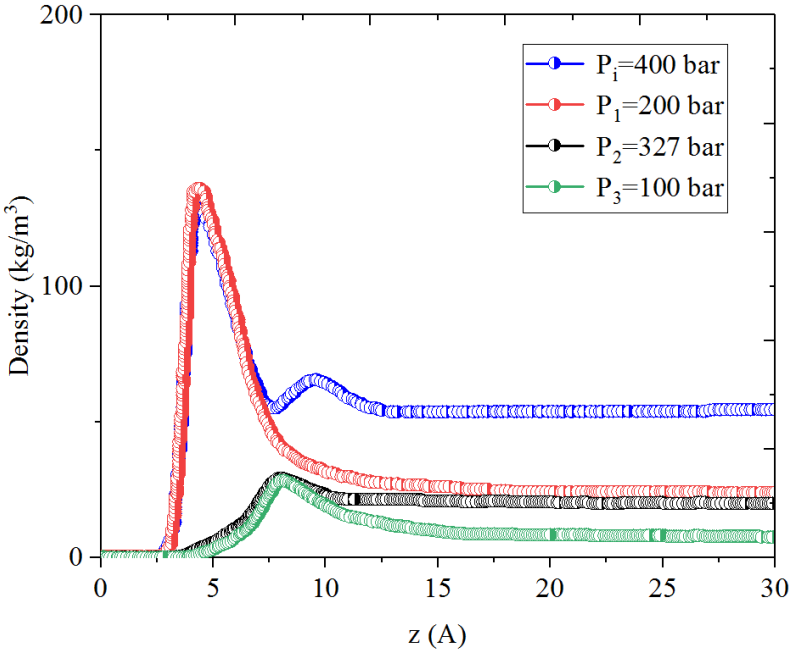

Figure 14. Density profiles of C_4H_{10} in CH_4-C_4H_{10}-CO_2 mixture in inorganic mesopores at P_i, P_1, P_2, and P_3, respectively.

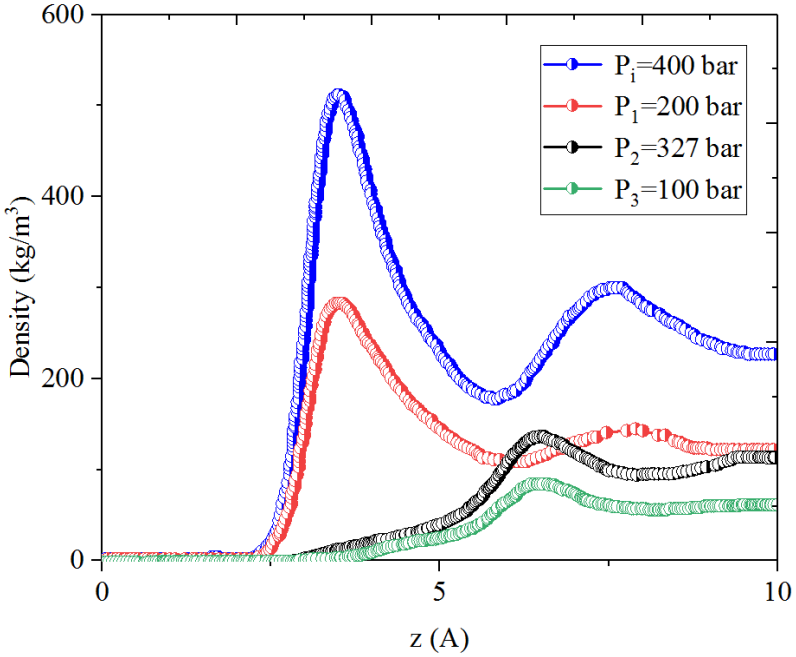

Figure 15. Density profiles of CH_4 in CH_4-C_4H_{10}-CO_2 mixture in inorganic micropores at P_i, P_1, P_2, and P_3, respectively.

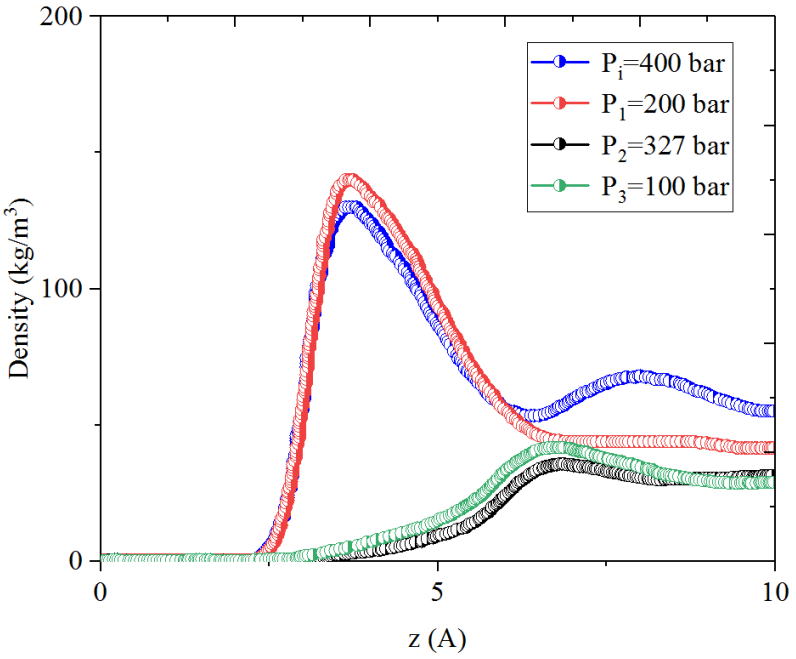

Figure 16. Density profiles of C_4H_{10} in CH_4-C_4H_{10}-CO_2 mixture in inorganic micropores at P_i, P_1, P_2, and P_3, respectively.

3.3. Shale Hydrocarbon Recovery

The oil recovery efficiency (*RE*) is obtained for CH_4 and C_4H_{10} from the organic and inorganic micro- and mesopores. *RE* is calculated by $\int_{z_0}^{z_i} \rho_{P_i} dv / \int_{z_0}^{z'_0} \rho_{P_0} dv$ (where ρ_{P_i} and ρ_{P_0} represent the density profiles at P_i and P_0). Figures 17–20 present the recovery efficiency during pressure drawdown and the CO_2 huffing and puffing period. We find that RE during pressure drawdown is smaller in micropores than in mesopores, and vice versa for the heavier hydrocarbons, i.e., C_4H_{10}. In inorganic pores, the recovery efficiency of C_4H_{10} is much higher than that of organic pores. However, RF is comparable in both kinds

of pores for the lighter hydrocarbons, i.e., CH_4. Interestingly, the recovery efficiency for C_4H_{10} can be negative in the micropores during pressure drawdown; in other words, the heavy hydrocarbons tend to accumulate in the small pores as pressure drops, which is in line with our previous findings. During CO_2 huff and puff, the recovery efficiency of CH_4 is higher in the organic pores than that of the inorganic pores; the efficiency during the CO_2 huffing process is comparable in the micro- and mesopores. More importantly, we observe that the recovery efficiency of C_4H_{10} reaches the highest in both the inorganic and organic pores during the CO_2 huff and puff process. It suggests that the CO_2 huff and puff method is more suitable for heavier hydrocarbon recovery compared to the pressure drawdown method.

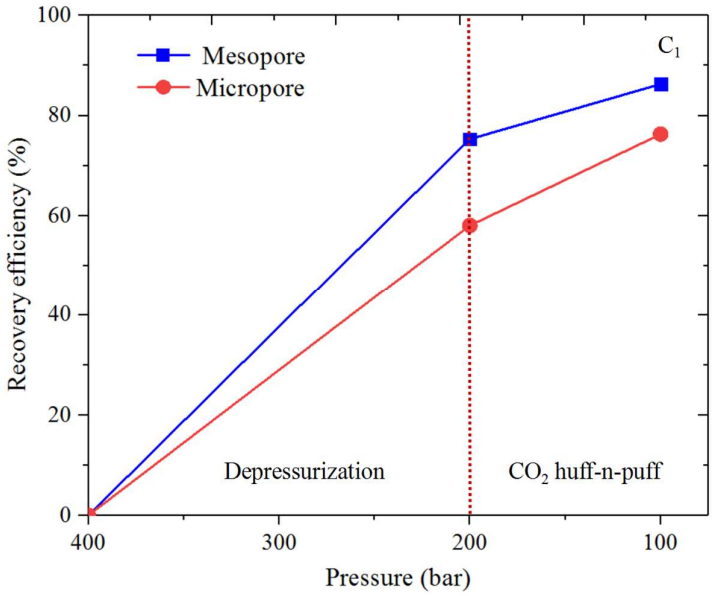

Figure 17. Recovery efficiency of CH_4 from the organic nanopores during pressure drawdown and the CO_2 huff and puff process.

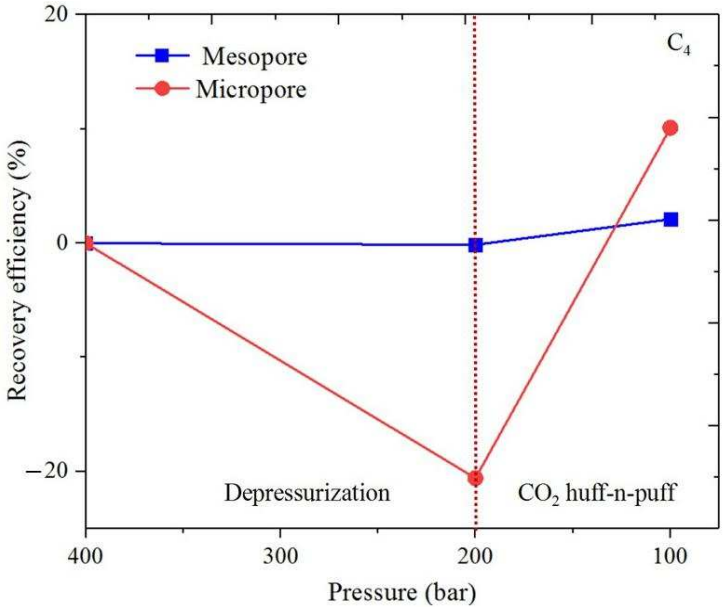

Figure 18. Recovery efficiency of C_4H_{10} from the organic nanopores during pressure drawdown and the CO_2 huff and puff process.

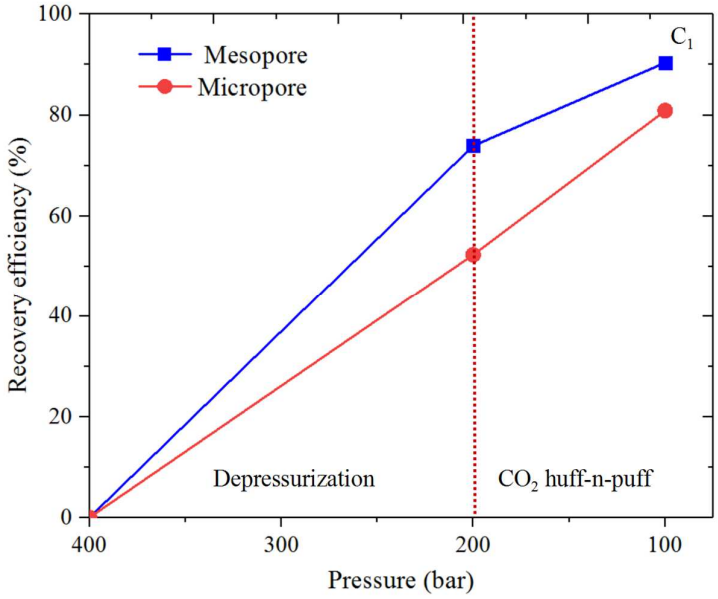

Figure 19. Recovery efficiency of CH_4 from the inorganic nanopores during pressure drawdown and the CO_2 huff and puff process.

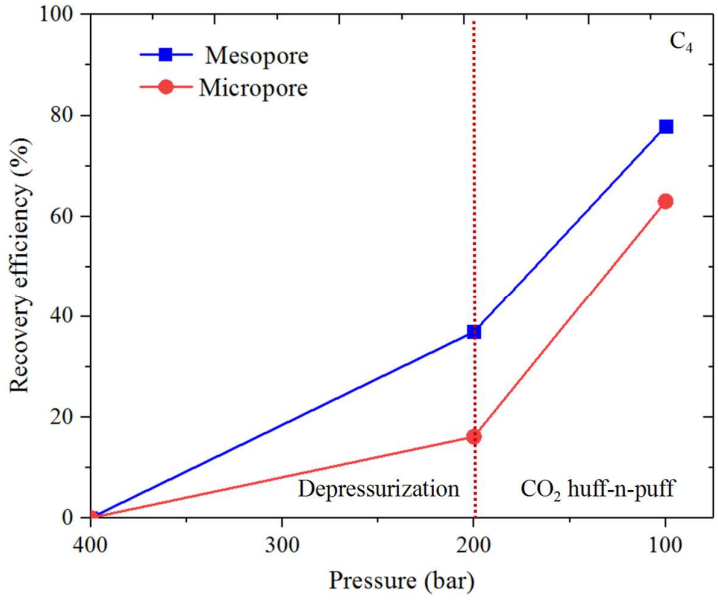

Figure 20. Recovery efficiency of C_4H_{10} from the inorganic nanopores during pressure drawdown and the CO_2 huff and puff process.

3.4. CO_2 Sequestration in Nanopores

Figures 21 and 22 present the molar fraction of the free-state and adsorbed-state CO_2 in the micro- and meso-organic and -inorganic pores, respectively. In the organic pores, CO_2 is mainly sequestrated in the adsorbed state in micropores, while, in the mesopores, free-state CO_2 dominates at low pressures. In large pores, most CO_2 molecules are adsorbed on the pore surface during high-pressure conditions; however, as pressure decreases, the adsorbed CO_2 desorbs from the pore surface and is sequestrated in the free state. Comparatively, in the small pores, CO_2 molecules are mainly in adsorbed state storage due to the strong fluid–pore surface interactions. In the inorganic pores, CO_2 is stored mainly in the free state due to the relatively weak fluid–pore surface interactions, except in the micropores at high-pressure conditions. Similarly, as pressure decreases, CO_2 sequestration transfers from the adsorbed state to the free-gas state in the inorganic pores. In summary, CO_2

sequestration in the adsorbed state is safer than that in the free state. A high content of organic matter, high pressure, and small pores are beneficial factors for transforming CO_2 sequestration into adsorbed state storage.

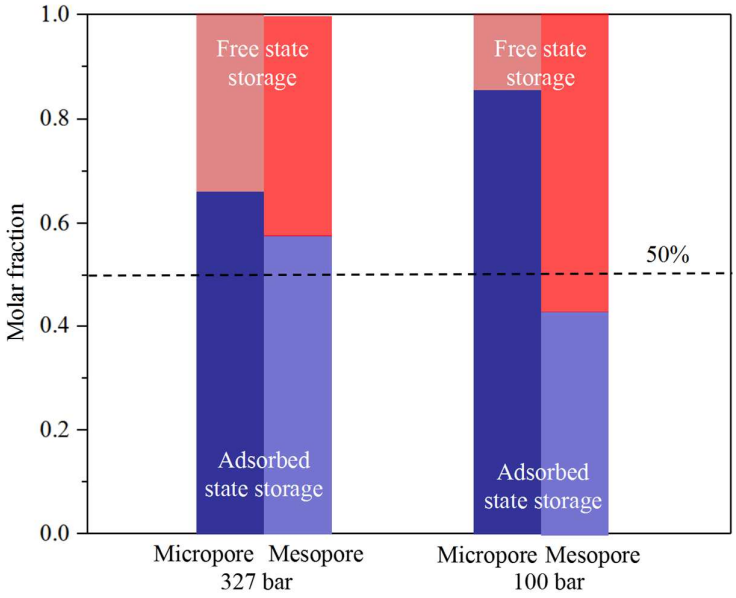

Figure 21. The molar fraction of the free-state and adsorbed-state CO_2 in the micro- and meso-organic pores.

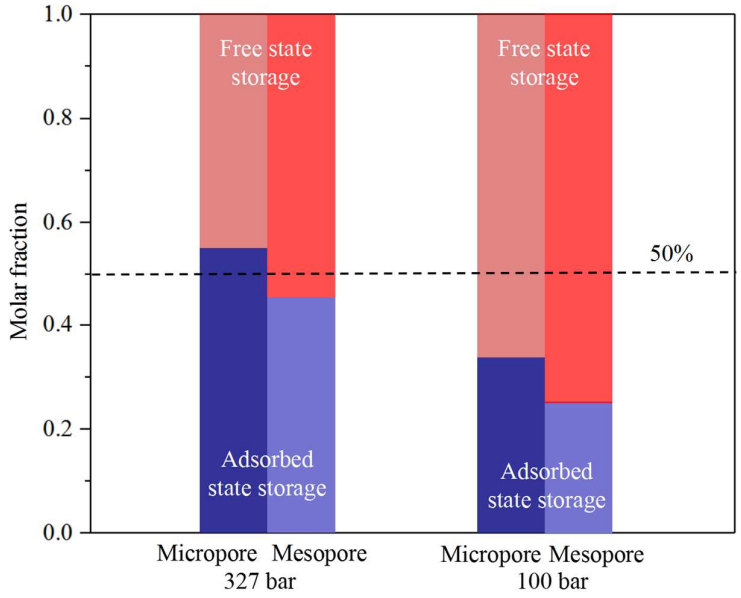

Figure 22. The molar fraction of the free-state and adsorbed-state CO_2 in the micro- and meso-inorganic pores.

4. Conclusions

In this work, the GCMC simulation methods were applied to study the mechanisms of shale hydrocarbon extraction in organic and inorganic nanopores with sizes of 1 nm and 3 nm, analyzing the impact of pressure drawdown and the CO_2 huff and puff process on gas recovery rates. During the primary gas production, CH_4 readily desorbs from the pore surface and is produced as reservoir pressure drops. On the contrary, C_4H_{10} tends to be trapped in these organic nanopores and is difficult to produce, especially in the micropores. Comparatively, it is more difficult to recover C_4H_{10} from the inorganic pores. During

the CO_2 puffing process, the adsorbed CH_4 desorbs from the pore surface continuously and can therein be heavily extracted. However, the adsorbed C_4H_{10} cannot be readily produced. During the CO_2 huffing period, the adsorbed CH_4 and C_4H_{10} can desorb and escape from the inorganic mesopores, enhancing shale gas production. However, during the CO_2 puffing period, C_4H_{10} in the inorganic micropores is hard to recover. Research findings indicate that during pressure drawdown and the CO_2 huff and puff process, CH_4 is more easily desorbed and released from the pores, whereas C_4H_{10} is more difficult to generate and recover, especially in inorganic micropores.

Recovery efficiency during pressure drawdown is smaller in micropores than that of the mesopores. In inorganic pores, the recovery efficiency of C_4H_{10} is much higher than that in the organic pores. However, it is comparable in both pores for CH_4. In addition, the recovery efficiency of C_4H_{10} can be negative in the micropores during pressure drawdown. During CO_2 huff and puff, the recovery efficiency of CH_4 is higher in the organic pores than that in the inorganic pores. More importantly, the recovery efficiency of C_4H_{10} reaches the highest for both the inorganic and organic pores during the CO_2 huff and puff process. These findings indicate that the CO_2 huff and puff method is more effective for recovering heavier hydrocarbons than the pressure drawdown method.

Beyond traditional carbon sequestration methods, CO_2 mainly sequestrates in the adsorbed state in organic pores, while it mainly sequestrates in the free-gas state in the inorganic pores. According to the content of this study, CO_2 sequestration in the adsorbed state is safer than that in the free state. In our work, it is found that a high content of organic matter, high pressure, and small pores are beneficial factors for CO_2 sequestration transforming into adsorbed state storage.

Author Contributions: Data curation and Writing–original draft, J.G.; Formal analysis and Project administration, S.K.; Investigation, K.L.; Methodology, G.R.; Software, T.Y.; Supervision, K.D.; Writing-review & editing and Funding acquisition, Y.L. All authors have read and agreed to the published version of the manuscript.

Funding: This research was funded by the National Natural Science Foundation of China (Grant No. 52004320), the PetroChina Innovation Foundation (2019D-5007-0204), and the Science Foundation of China University of Petroleum, Beijing (No. 2462021QNXZ012). Additionally, funding was received from the Science and Technology Innovation Project of the Shanxi Provincial Department of Education for the study on the multi-field coupling and multi-phase reaction mechanism of solid waste filling and sealing of goaf in power plants and coal mines (No.: 2022SX55L055), as well as from a youth project of the Shanxi Basic Research Program (Free Exploration) for research on the multi-field coupling mechanism of solid waste filling and simultaneous storage of CO_2 in goaf (No.: 2022SX09301223073). Furthermore, support was provided by the Hebei Provincial Natural Science Foundation Funded Project–Outstanding Young Scientist Fund Project (E2023508019). The APC was funded by [a youth project of the Shanxi Basic Research Program (Free Exploration)].

Data Availability Statement: We do not accept the public sharing of raw data. The raw data discussed in this study is included in the article materials, and further inquiries can be directed to the corresponding author.

Conflicts of Interest: Author Guoan Ren was employed by the company Jin Chuang Investment, The remaining authors declare that the research was conducted in the absence of any commercial or financial relationships that could be construed as a potential conflict of interest.

References

1. Cao, Y.; Jin, Z.; Zhu, R.; Liu, K. Pore systems and their correlation with oil enrichment in various lithofacies of saline lacustrine shale strata. *Int. J. Coal Geol.* **2024**, *282*, 104444. [CrossRef]
2. EIA. *Annual Energy Outlook 2017 with Projections to 2050*; EIA: San Antonio, TX, USA, 2017.
3. Jia, B.; Tsau, J.S.; Barati, R. A review of the current progress of CO_2 injection EOR and carbon storage in shale oi reservoirs. *Fuel* **2019**, *236*, 404–427. [CrossRef]
4. Flannery, J.; Kraus, J. Integrated Analysis of the Bakken Petroleum System. *Am. Assoc. Pet. Geol. Search Discov.* **2006**, *19*, 138–145.
5. Hamling, Z. Developments in CO_2, ethane, and rich gas EOR: A Williston basin perspective. In Proceedings of the CO_2 & ROZ Conference Carbon Management Workshop, Midland, TX, USA, 4 December 2017.

6. Ahmed, U.; Meehan, D.N. *Unconventional Oil and Gas Resources: Exploitation and Development*; Taylor & Francis: Abingdon, UK, 2016.
7. Liu, Y.; Jin, Z.; Li, H. Comparison of Peng-Robinson equation of state with capillary pressure model with engineering density-functional theory in describing the phase behavior of confined hydrocarbons. *SPE J.* **2018**, *23*, 1784–1797. [CrossRef]
8. Yu, W.; Lashgari, H.R.; Wu, K.; Sepehrnoori, K. CO_2 injection for enhanced oil recovery in Bakken tight oil reservoirs. *Fuel* **2015**, *212*, 321–435. [CrossRef]
9. Cherian, B.V.; Stacey, E.S.; Lewis, R.; Iwere, F.O.; Heim, R.N.; Higgins, S.M. Evaluating horizontal well completion effectiveness in a field development program. SPE 152177. Presented at SPE Hydraulic Fracturing Technology Conference, The Woodlands, TX, USA, 6–8 February 2012; p. 506.
10. Hoffman, B.T. Comparison of various gases for enhanced recovery from shale oil reservoirs. SPE 154329. Presented at SPE Improved Oil Recovery Symposium, Tulsa, OK, USA, 14–18 April 2012.
11. Hawthorne, S.B.; Gorecki, C.D.; Sorensen, J.A.; Steadman, E.N.; Harju, J.A.; Melzer, S. Hydrocarbon mobilization mechanisms from upper, middle, and lower Bakken reservoir rocks exposed to CO_2. SPE 167200. Presented at SPE Unconventional Resources Conference, Calgary, AB, Canada, 5–7 November 2013.
12. Stalkup, F.I. Displacement behavior of the condensing/vaporizing gas drive process. SPE 16715. Presented at SPE Annual Technical Conference and Exhibition, Dallas, TX, USA, 27–30 September 1987.
13. Holm, L.W. Evolution of the carbon dioxide flooding processes. *J. Petrol. Technol.* **1987**, *39*, 1337–1342. [CrossRef]
14. Kurtoglu, B.; Sorensen, J.A.; Braunberger, J.; Smith, S.; Kazemi, H. Geologic characterization of a Bakken reservoir for potential CO_2 EOR. SPE 168915. Presented at Unconventional Resources Technology Conference, Denver, CO, USA, 12–14 August 2013.
15. Song, C.; Yang, D. Performance evaluation of CO_2 huff-n-puff processes in tight oil formations. SPE 167217. Presented at SPE Unconventional Resources Conference, Calgary, AB, Canada, 5–7 November 2013.
16. Adekunle, O.; Hoffman, B.T. Minimum miscibility pressure studies in the Bakken. SPE 169077. Presented at SPE Improved Oil Recovery Symposium, Tulsa, OK, USA, 12–16 April 2014.
17. Jarrell, P.M.; Fox, C.E.; Stein, M.H.; Webb, S.L. *Practical Aspects of CO_2 flooding: SPE Monograph, Vol. 22. Henry L. Doherty Series*; Society of Petroleum Engineers: Richardson, TX, USA, 2002.
18. Holm, L.W.; Josendal, V.A. Mechanisms of oil displacement by carbon dioxide. *J. Petrol. Technol.* **1974**, *26*, 1427–1438. [CrossRef]
19. Zhang, M.; Zhan, S.; Zhan, S.; Jin, Z. Recovery mechanisms of hydrocarbon mixtures in organic and inorganic nanopores during pressure drawdown and CO_2 injection from molecular perspectives. *Chem. Eng. J.* **2020**, *382*, 122808. [CrossRef]
20. Xu, H.; Kim, D.H.; Delshad, M. Potential for non-thermal cost-efective chemical augmented waterflood for viscous oils. Paper SPE 165350. Presented at the SPE Western Regional and AAPG Pacific Section Meeting Joint Technical Conference, Monterey, CA, USA, 19–25 April 2012.
21. Fortenberry, R. Experimental Demonstration and Improvement of Chemical EOR Techniques in Heavy Oils. Master Thesis, University if Texas at Austin, Austin, TX, USA, 2013.
22. Tagavifar, M.; Fortenberry, R.; Rouffignac, E.D.; Sepehrnoori, K.; Pope, G. Heavy oil recovery by combined hot water and alkali/cosolvent/polymer flooding. *SPE J.* **2016**, *21*, 74–86. [CrossRef]
23. Liu, Y.; Hu, T.; Rui, Z.; Zhang, Z.; Du, K.; Yang, T.; Dindoruk, B.; Stenby, E.H.; Torabi, F.; Afanasyev, A. An Integrated Framework for Geothermal Energy Storage with CO_2 Sequestration and Utilization. *Engineering*, 2023; *in press*.
24. Al-Anazi, H.A.; Walker, J.G.; Pope, G.A.; Sharma, M.M.; Hackney, D.F. A successful methanol treatment in a gas/condensate reservoir: Field application. *SPE Prod. Fac.* **2003**, *20*, 60–69. [CrossRef]
25. Sayed, M.A.; Al-Muntasheri, G.A. Liquid bank removal in production wells drilled in gas-condensate reservoirs: A critical review. In Proceedings of the SPE International Symposium and Exhibition on Formation Damage Control, Lafayette, LA, USA, 19–21 February 2020; pp. 26–28.
26. Liu, Y.; Rui, Z. A Storage-driven CO_2 EOR for net-zero emission target. *Engineering* **2022**, *18*, 79–87. [CrossRef]
27. Liu, Y.; Rui, Z.; Dindoruk, B.; Yang, T. Using propanol as an additive to CO_2 for improving CO_2 utilization and storage in oil reservoirs. *Appl. Energy* **2022**, *311*, 118640. [CrossRef]
28. Cao, Y.; Jin, Z.; Zhu, R.; Liu, K.; Bai, J. Comprehensive evaluation of the organic-rich saline lacustrine shale in the Lucaogou Formation, Jimusar sag, Junggar Basin, NW China. *Energy* **2024**, *294*, 130786. [CrossRef]
29. Etminan, S.R.; Maini, B.B.; Chen, Z.; Hassanzadeh, H. Constant-pressure technique for gas diffusivity and solubility measurements in heavy oil and bitumen. *Energy Fuels* **2010**, *24*, 533–549. [CrossRef]
30. Sigmund, P.M. Prediction of molecular diffusion at reservoir conditions. Part 1—measurement and prediction of binary dense gas diffusion coefficients. *J. Can. Pet. Technol.* **1976**, *15*, 48–57. [CrossRef]
31. Ghaderi, S.M.; Tabatabaie, S.H.; Hassanzadeh, H.; Pooladi-Darvish, M. Estimation of concentration-dependent diffusion coefficient in pressure-decay experiment of heavy oils and bitumen. *Fluid Phase Equilib.* **2011**, *305*, 132–144. [CrossRef]
32. Riazi, M.R.; Whitson, C.H. Estimating diffusion coefficients of dense fluids. *Ind. Eng. Chem. Res.* **1993**, *32*, 3081–3088. [CrossRef]
33. Jiang, J.; Rui, Z.; Hazlett, R.; Lu, J. An integrated technical-economic model for evaluating CO_2 enhanced oil recovery development. *Appl. Energy* **2019**, *247*, 190–211. [CrossRef]
34. Zhao, Y.; Rui, Z.H.; Zhang, Z.; Chen, S.W.; Yang, R.F.; Du, K.; Dindoruk, B.; Yang, T.; Stenby, E.H.; Wilson, M.A. Importance of conformance control in reinforcing synergy of CO_2 EOR and sequestration. *Pet. Sci.* **2022**, *19*, 3088–3106. [CrossRef]

35. Song, L.; Kantzas, A.; Bryan, J.L. Experimental measurement of diffusion coefficient of CO_2 in heavy oil using X-ray computed-assisted tomography under reservoir conditions. In Proceedings of the SPE Canadian Unconventional Resources and International Petroleum Conference, Calgary, AB, USA, 19–21 October 2010.
36. Liu, Y.; Ma, X.; Hou, J. Comparing the effectiveness of SO_2 with CO_2 for replacing hydrocarbons from nanopores. *Energy Fuels* **2019**, *33*, 5200–5207. [CrossRef]
37. Huang, X.; Gu, L.; Li, S.; Du, Y.; Liu, Y. Absolute adsorption of light hydrocarbons on organic-rich shale: An efficient determination method. *Fuel* **2022**, *308*, 121998. [CrossRef]
38. Liu, Y.; Ma, X.; Li, H.; Hou, J. Competitive adsorption behavior of hydrocarbon(s)/CO_2 mixtures in a double-nanopore system using molecular simulations. *Fuel* **2019**, *252*, 612–621. [CrossRef]
39. Deer, W.A.; Howie, R.A.; Zussman, J. *An Introduction to the Rock Forming Minerals*; Longman: London, UK, 1996.
40. Fernández, J.; Sotenko, M.; Derevschikov, V.; Lysikov, A.; Rebrov, E.V. A radiofrequency heated reactor system for post-combustion carbon capture. *Chem. Eng. Process. Process Intensif.* **2016**, *108*, 17–26. [CrossRef]
41. Chronopoulos, T.; Fernandez-Diez, Y.; Maroto-Valer, M.M.; Ocone, R.; Reay, D.A. CO_2 desorption via microwave heating for post-combustion carbon capture. *Microporous Mesoporous Mater.* **2014**, *197*, 288–290. [CrossRef]
42. Szczerba, M.; Derkowski, A.; Kalinichev, A.G.; Środoń, J. Molecular modeling of the effects of 40Ar recoil in illite particles on their K-Ar isotope dating. *Geochim. Cosmochim. Acta* **2015**, *159*, 162–176. [CrossRef]
43. Martin, M.G.; Siepmann, J.I. Transferable potentials for phase equilibria. 1. United-atom description of n-alkanes. *J. Phys. Chem. B* **1998**, *102*, 2569–2577. [CrossRef]
44. Lorentz, H.A. Nachtrag zu der Abhandlung: Ueber die Anwendung des Satzes vom Virial in der kinetischen Theorie der Gase. *Ann. Phys* **1881**, *248*, 660–661. [CrossRef]
45. Jin, Z.; Firoozabadi, A. Effect of water on methane and carbon dioxide sorption in clay minerals by Monte Carlo simulations. *Fluid Phase Equilibria* **2014**, *382*, 10–20. [CrossRef]
46. Crozier, P.S.; Rowley, R.L.; Spohr, E.; Henderson, D. Comparison of charged sheets and corrected 3D Ewald calculations of long-range forces in slab geometry electrolyte systems with solvent molecules. *J. Chem. Phys.* **2000**, *112*, 9253–9257. [CrossRef]
47. Liu, Y.; Li, H.A.; Tian, Y.; Jin, Z.; Deng, H. Determination of the absolute adsorption/desorption isotherms of CH_4 and n-C_4H_{10} on shale from a nano-scale perspective. *Fuel* **2018**, *218*, 67–77. [CrossRef]
48. Hensen EJ, M.; Tambach, T.J.; Bliek, A.; Smit, B. Adsorption isotherms of water in Li-, Na-, and K-montmorillonite by molecular simulations. *J. Chem. Phys.* **2001**, *115*, 3322–3329. [CrossRef]
49. Widom, B. Some topics in the theory of fluids. *J. Chem. Phys.* **1963**, *39*, 2808–2812. [CrossRef]
50. Peng, D.-Y.; Robinson, D.B. A new two-constant equation of state. *Ind. Eng. Chem. Fundam.* **1976**, *15*, 59–64. [CrossRef]
51. Lu, L.; Wang, Q.; Liu, Y. Adsorption and separation of ternary and quaternary mixtures of short linear alkanes in zeolites by molecular simulation. *Langmuir* **2003**, *19*, 10617–10623. [CrossRef]
52. Sun, Z.; Wu, K.; Shi, J.; Zhang, T.; Feng, D.; Huang, L.; Li, X. An analytical model for transport capacity of water confifined in nanopores. *Int. J. Heat Mass Transf.* **2019**, *138*, 620–630. [CrossRef]
53. Yu, X.; Tang, W.; Zhao, T.; Jin, Z.; Zhao, S.; Liu, H. Confinement effect on molecular conformation of alkanes in water-filled cavitands: A combined quantum/classical DFT study. *Langmuir* **2018**, *34*, 13491–13496. [CrossRef]
54. Baek, S.; Akkutlu, I.Y. Produced-flfluid composition redistribution in source rocks for hydrocarbon-in-place and thermodynamic recovery calculations. *SPE J.* **2019**, *24*, 1395–1414. [CrossRef]
55. Buckingham, A.; Disch, R.-L. The quadrupole moment of the carbon dioxide molecule. *Proc. R. Soc. Lond. A* **1963**, *273*, 275–289.
56. Sethia, G.; Somani, R.S.; Bajaj, H.C. Adsorption of carbon monoxide, methane and nitrogen on alkaline earth metal ion exchanged zeolite-X: Structure, cation position and adsorption relationship. *RSC Adv.* **2015**, *5*, 12773–12781. [CrossRef]

Disclaimer/Publisher's Note: The statements, opinions and data contained in all publications are solely those of the individual author(s) and contributor(s) and not of MDPI and/or the editor(s). MDPI and/or the editor(s) disclaim responsibility for any injury to people or property resulting from any ideas, methods, instructions or products referred to in the content.